CrystEngComm

PAPER

View Article Online
View Journal | View Issue

Controlled overgrowth of Pd on Au nanorods†

Cite this: *CrystEngComm*, 2014, **16**, 9469

Hao Jing and Hui Wang*

In this paper, we present a detailed, systematic study of the controlled overgrowth of Pd on Au nanorods. Pd nanoshells with fine-controlled dimensions and architectures were overgrown on single-crystalline Au nanorods through seed-mediated growth using H_2PdCl_4 as the Pd precursor and ascorbic acid as the reducing agent in the presence of cetyltrimethylammonium chloride (CTAC) or cetyltrimethylammonium bromide (CTAB) as the surface capping agent. The effects of surface capping agent, ascorbic acid to H_2PdCl_4 ratio, reaction temperature, and structure-directing foreign ions, such as Ag^+, on the dimensions and architectures of the resulting Au@Pd core–shell heteronanostructures were systematically studied. At 30 °C, Au nanorods coated with polycrystalline Pd shells were obtained using CTAC as the surface capping agent, while single-crystalline Au@Pd core–shell nanocuboids formed in the presence of CTAB. The thicknesses of the polycrystalline and single-crystalline Pd shells were fine-controlled by adjusting the molar ratio of ascorbic acid to H_2PdCl_4. At an elevated reaction temperature of 60 °C, irregularly shaped and cylindrical co-axial core–shell nanorods were obtained in CTAC and CTAB, respectively. By introducing Ag^+ ions into the Pd growth solution, Au nanorods coated with segregated Pd nanoislands and dumbbell-like core–shell heteronanostructures were obtained as a consequence of the underpotential deposition of Ag and sustainable galvanic replacements that concurred during the Pd overgrowth processes. The effects of the Pd shell dimensions and morphologies on the plasmonic properties of the Au@Pd core–shell nanostructures were also investigated.

Received 24th March 2014,
Accepted 25th April 2014

DOI: 10.1039/c4ce00601a

www.rsc.org/crystengcomm

1. Introduction

Bimetallic heteronanostructures have emerged as an important class of multifunctional nanomaterials with synergistic optical, electronic, and catalytic properties that are drastically different from those of their monometallic analogues.[1–4] Au and Pd, in particular, represent an interesting combination of noble metals for the construction of multifunctional bimetallic hetero-nanostructures owing to the intriguing plasmonic properties of Au and the great catalytic performance of Pd.[5–11] Seed-mediated nanocrystal growth provides a robust and versatile approach to the deposition of Pd onto Au nanoparticles to form hybrid bimetallic heteronanostructures with fine-controlled sizes, shapes, compositions, and surfaces.[12–22] Through manipulation of the kinetic and thermodynamic parameters governing the nanocrystal growth, architecturally controlled Pd can be deposited either conformally or in a site-selective manner on the surface of the Au seeds,[12–22] allowing one to delineate how the particle geometries, the interfacial structures, and the spatial arrangements of the constituent domains influence the synergistic properties of the bimetallic heteronanostructures.

Au nanorods represent an interesting subwavelength photonic nanostructure with highly tunable plasmon resonances over a broad spectral range across the visible and near-infrared regions.[23–25] Controlled deposition of Pd onto Au nanorods further enhances our capabilities of fine-tuning the plasmonic properties of the heteronanostructures. Coating a Au nanorod with a thin layer of Pd significantly enhances the particle's plasmonic sensitivity to the refractive index of the surrounding medium,[26] making the Au@Pd core–shell nanorods more sensitive for refractometric biosensing than the monometallic Au nanorods. An interesting plasmonic percolation behaviour was recently observed on Au@Pd core–shell nanorods when discontinuous Pd islands merged into a continuous shell on the surface of the Au nanorod cores.[27] Overgrowth of Pd on Au nanorods also provides a unique approach to the incorporation of catalytic activities into plasmonically tunable nanostructures.[28,29] It was recently demonstrated that Au nanorods with Pd nanocrystals deposited at the tips exhibited dual functionality for both plasmon-mediated light harvesting and highly efficient catalysis for Suzuki cross-coupling reactions.[28] More recently, Au nanorods with Au–Pd alloy nanohorns epitaxially grown at the tips showed unique capability of coupling high catalytic activity with strong local field

Department of Chemistry and Biochemistry, University of South Carolina, 631 Sumter Street, Columbia, South Carolina 29208, USA.
E-mail: wang344@mailbox.sc.edu; Fax: +1 803 777 9521; Tel: +1 803 777 2203

† Electronic supplementary information (ESI) available: Additional figures as noted in the text. See DOI: 10.1039/c4ce00601a

enhancements,[29] enabling accurate measurements of the kinetics of 4-nitrothiophenol hydrogenation using surface-enhanced Raman spectroscopy (SERS).

The fine-control over the growth of Pd on Au nanorods allows one to judiciously tailor the particle architectures and thereby fine-tune the optical and catalytic properties of the bimetallic heteronanostructures. Under facile ambient conditions, a polycrystalline layer composed of discrete Pd nanocrystals can be assembled on the surface of Au nanorods through seed-mediated electroless deposition of Pd.[30] By deliberately tuning the deposition parameters, it has been shown that Pd can also be grown epitaxially on Au nanorods to form conformal core–shell nanorods with a single crystalline structure.[31,32] In addition, introducing halide anions, such as I^-, into the Pd growth solutions allows for the regulation of the relative growth rates along various crystalline facets, resulting in the selective formation of cuboidal and elongated tetrahexahedral Au@Pd core–shell nanoparticles.[33] Furthermore, the crystalline structures of the Au nanorod cores also play a key role in guiding the overgrowth of the Pd shells. It was recently found that Pd grew preferentially on the side facets of single-crystalline Au nanorods, whereas it grew selectively on the ends of multi-twined Au nanorods.[34]

In this paper, we report a detailed and systematic study of the controlled overgrowth of Pd on single-crystalline Au nanorods using H_2PdCl_4 as the Pd precursor, ascorbic acid (AA) as the reducing agent, and cetyltrimethylammonium chloride (CTAC) or cetyltrimethylammonium bromide (CTAB) as the surface capping agent, respectively. We demonstrate that the dimensions and architectures of the deposited Pd shells can be fine-controlled by adjusting several important experimental parameters, such as the surface capping agents, molar ratios of AA to H_2PdCl_4, reaction temperatures, and structure-directing foreign ions. The mechanisms of the Pd overgrowth on Au nanorods under various experimental conditions were discussed.

2. Experimental section

2.1 Chemicals

All chemicals were commercially available and used as received without further purification. CTAB (>98.0%) and sodium oleate (NaOL, >97.0%) were purchased from TCI America. Hydrogen tetrachloroaurate trihydrate ($HAuCl_4{\cdot}3H_2O$, 99.99% metals basis), silver nitrate ($AgNO_3$, 99.9995% metals basis), and CTAC (96% powder) were purchased from Alfa Aesar. L-ascorbic acid (BioUltra, ≥99.5%), sodium borohydride ($NaBH_4$, 99%), hydrochloric acid (HCl, 37 wt% in water), and palladium(II) chloride ($PdCl_2$, ≥99.9%) were purchased from Sigma Aldrich. Ultrapure water (18.2 MΩ resistivity, Barnstead EasyPure II 7138) was used for all experiments. 10 mM H_2PdCl_4 solution was prepared by dissolving 44.5 mg of $PdCl_2$ in 25 mL of 10 mM HCl. All glassware was cleaned using freshly prepared aqua regia ($HCl:HNO_3$ in a 3 : 1 ratio by volume) followed by thorough rinse with copious amount of water.

2.2 Synthesis of Au nanorods

Au nanorods were prepared using a seed-mediated growth method[35] with some slight modifications. To prepare the seed solution for Au nanorod growth, 5 mL of 0.5 mM $HAuCl_4$ was first mixed with 5 mL of 0.2 M CTAB solution in a 20 mL scintillation vial. Then 1 mL of freshly prepared 6 mM $NaBH_4$ was quickly injected into the Au(III)–CTAB solution under vigorous magnetic stir (1200 rpm). The solution colour changed from yellow to brownish-yellow, and the stir was stopped after 2 min. The seed solution was aged at room temperature for 30 minutes before use.

To prepare the nanorod growth solution, 7.0 g CTAB together with 1.234 g NaOL were dissolved in 250 mL of water at 60 °C in a 500 mL Erlenmeyer flask. After the solution was cooled to 30 °C, 24 mL of 4 mM $AgNO_3$ was added. The mixture was kept undisturbed at 30 °C for 15 min, followed by the addition of 250 mL of 1 mM $HAuCl_4$. After magnetic stir at 700 rpm for 90 min, 4.8 mL of 37 wt% HCl was introduced to adjust pH. After another 15 min of slow stir at 400 rpm, 1.25 mL of 64 mM AA was added and the solution was vigorously stirred for 30 s. Finally, 0.4 mL seed solution was injected into the growth solution. The reactant mixture was vigorously stirred (1200 rpm) for another 30 s and left undisturbed at 30 °C for 12 h. The resulting Au nanorods were centrifuged, washed with water twice, and finally redispersed in 50 mL of 0.1 M CTAC or CTAB for future use.

2.3 Controlled overgrowth of Pd on Au nanorods

Au@Pd core–shell heteronanostructures with architecturally controlled Pd shells were fabricated through controlled overgrowth of Pd on Au nanorods. Briefly, 200 μL of colloidal Au nanorods dispersed in 0.1 M CTAC or CTAB was first diluted to 2 mL with water. Then 300 μL of 10 mM H_2PdCl_4 and various volumes of 50 mM AA were added. The reaction mixtures were kept in a water bath either at 30 °C or 60 °C and left undisturbed for 12 h. The products were centrifuged, washed with water twice, and finally redispersed in 0.5 mL of water.

2.4 Ag^+-mediated overgrowth of Pd on Au nanorods

200 μL of colloidal Au nanorods dispersed in 0.1 M CTAC or 0.1 M CTAB was diluted to 2 mL with water. Then 300 μL of 10 mM H_2PdCl_4 and 400 μL of 1 mM $AgNO_3$ were added simultaneously into the mixture under magnetic stir at 700 rpm, followed by the addition of 30 μL of 50 mM AA. The reaction mixtures were kept in a water bath at 30 °C and left undisturbed for 12 h to grow discrete Pd nanoislands on the surface of the Au nanorods.

2.5 Fabrication of Au@Pd core–shell nanodumbbells

Au nanorods coated with a thin layer of Ag were first synthesized through underpotential deposition (UPD) of Ag on Au nanorods. Briefly, 200 μL of colloidal Au nanorods dispersed in 0.1 M CTAC or 0.1 M CTAB was diluted to 2 mL with water. 400 μL of 1 mM $AgNO_3$ solutions were subsequently

added and the solution was mixed under magnetic stir for 10 min, followed by the addition of 30 μL of 50 mM AA. The reaction mixtures were kept in a water bath at 30 °C under magnetic stir (300 rpm) for 9 h. The resulting Au nanorods coated with Ag UPD layers were centrifuged and washed with water twice and then redispersed in 1.8 mL water, followed by the addition of 0.2 mL of 0.1 M CTAC or CTAB, 30 μL of 50 mM AA, and 300 μL of 10 mM H_2PdCl_4. The reactant mixtures were left undisturbed for 12 h at 30 °C to produce the dumbbell-shaped core–shell nanoparticles.

2.6 Nanostructure characterizations

The morphologies and structures of the bimetallic heteronanostructures were characterized by transmission electron microscopy (TEM) and selected area electron diffraction (SAED) using a Hitachi H-8000 transmission electron microscope, which was operated at an accelerating voltage of 200 kV. All samples for TEM measurements were dispersed in water and drop-dried on 300 mesh Formvar/Carbon coated-Cu grids (Electron Microscopy Science Inc.). The structures and compositions of the nanoparticles were also characterized by scanning electron microscopy (SEM) and energy-dispersive spectroscopy (EDS) using a Zeiss Ultraplus thermal field emission scanning electron microscope. The samples for SEM and EDS measurements were dispersed in water and drop-dried on silicon wafers. The optical extinction spectra of the nanoparticles were measured on aqueous colloidal suspensions at room temperature, using a Beckman coulter Du 640 spectrophotometer.

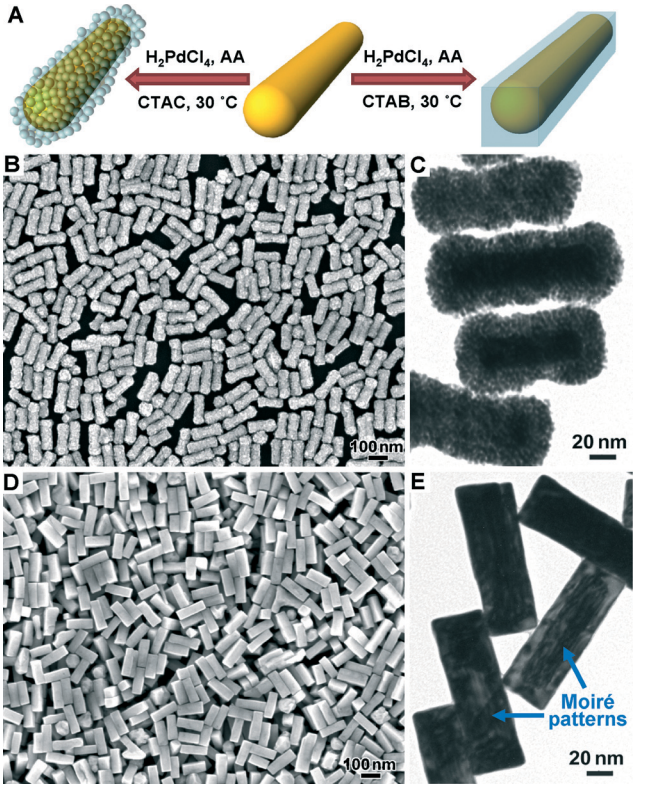

Fig. 1 (A) Schematic illustration of the overgrowth of Pd on Au nanorods at 30 °C in CTAC and CTAB, respectively. (B) SEM and (C) TEM images of Au@Pd core–shell nanorods with polycrystalline Pd shells formed in CTAC. (D) SEM and (E) TEM images of Au@Pd core–shell nanocuboids with conformal single-crystalline Pd shells formed in CTAB. The molar ratio of AA to H_2PdCl_4 was 1.0.

3. Results and discussions

3.1 Effects of surface capping agents on the morphologies of Au@Pd bimetallic heteronanostructures

Single-crystalline Au nanorods with a cylindrical morphology (see TEM and SEM images in Fig. S1 in ESI†) were employed as the cores that mediated the overgrowth of Pd shells. The as-fabricated Au nanorods were highly monodisperse with lengths of 95.8 ± 2.2 nm and widths of 24.2 ± 1.7 nm. The overgrowth of Pd on Au nanorods was conducted using AA as a weak reducing agent and H_2PdCl_4 as the Pd precursor in aqueous solution at 30 °C. As schematically illustrated in Fig. 1A, the Pd overgrowth in the presence of CTAC resulted in the formation of a polycrystalline Pd nanoshell on each Au nanorod, whereas Au@Pd core–shell nanocuboids with conformal single-crystalline Pd shells were obtained when CTAB was used as the surface capping agent. As shown in Fig. 1B and C, a large number of discrete ~3 nm Pd nanocrystals packed together to form a polycrystalline Pd shell surrounding the Au nanorod core. The lattice mismatch between Pd (0.389 nm) and Au (0.408 nm) is believed to be a key reason for the random nucleation of the Pd nanocrystallites on Au surfaces,[18,30] resulting in the formation of the polycrystalline shell structures. The polycrystalline nature of the Pd shells was further verified by the SAED pattern shown in Fig. S2A in ESI.† Interestingly, if CTAC was replaced with CTAB while the other experimental conditions were kept the same, Au@Pd core–shell nanocuboids enclosed by {100} facets were obtained as shown in Fig. 1D and E. These nanocuboids were single-crystalline in nature with well defined face-centered cubic (fcc) structures as shown by the SAED pattern in Fig. S2B in ESI.† Similar to previously reported single-crystalline Au@Pd core–shell nanocubes,[18] the SAED pattern of the nanocuboid was dominated by the electron diffraction features from the Pd shell. In the TEM image (Fig. 1E), the regions corresponding to the Au nanorod cores were covered with fringes composed of alternating bright and dark stripes. These fringes are known as Moiré patterns arising from the superposition of two mismatched crystalline lattices (Pd and Au lattices) that are aligned along the same direction.[17,18,36,37] The adsorption of CTAB on the Au nanorods resulted in the formation of a densely packed CTAB molecular bilayer on the Au surfaces[38] and thereby created a wetting layer at the Au–Pd interface to facilitate the expitaxial overgrowth in spite of the lattice mismatch. The formation of the cuboidal morphology was mainly attributed to the surface-energy minimization of the {100} facets and the suppression of the crystal growth perpendicular to the {100} facets due to the surface adsorption of CTAB.[31,34] Heteroepitaxial overgrowth of Pd was also observed on Au

nanospheres[17] and nanooctahedra[18] in the presence of CTAB, through which single-crystalline Au@Pd core–shell nanocubes were obtained.

The overgrowth of Pd should be adequately slow in order to form the expitaxial conformal Pd layers on Au.[18] The size evolution of the Au@Pd core–shell nanoparticles in CTAC and CTAB as a function of reaction time is shown in Fig. 2. TEM images of the samples obtained at different reaction times are shown in Fig. S3 and S4 in ESI.† The average widths and standard deviations of the core–shell nanoparticles were obtained by analyzing more than 200 particles in the TEM images for each sample. It is apparent that the growth of the polycrystalline Pd shells in CTAC was faster than that of the conformal, epitaxial Pd shells grown in CTAB. The slower shell growth in CTAB can be interpreted mostly likely as a consequence of the higher packing density of CTAB on Au nanorod surfaces than CTAC and the higher affinity of Br^- to the metal surfaces than that of Cl^-.[39]

3.2 Controlling the Pd shell thickness

The thicknesses of the polycrystalline and single-crystalline Pd shells could be fine-controlled by simply varying the molar ratios between AA and H_2PdCl_4. The cylindrical and cuboidal overall morphologies of the Au@Pd core–shell nanoparticles were both well-preserved as the Pd shell thickness varied, as shown in Fig. 3 and 4, respectively. The Pd overgrowth occurred both at the tips and on the side facets of the Au nanorods. As shown in Fig. 3G and 4G, the shell thickness progressively increased as the molar ratio of AA to the H_2PdCl_4 went up (the total amount of H_2PdCl_4 was fixed) until reaching a plateau when AA became excessive with respect to H_2PdCl_4. The polycrystalline Pd shells appeared to be thicker than the single-crystalline Pd shells at the same AA to H_2PdCl_4 ratios because of the lower packing density of the polycrystalline shells than the single-crystalline shells.

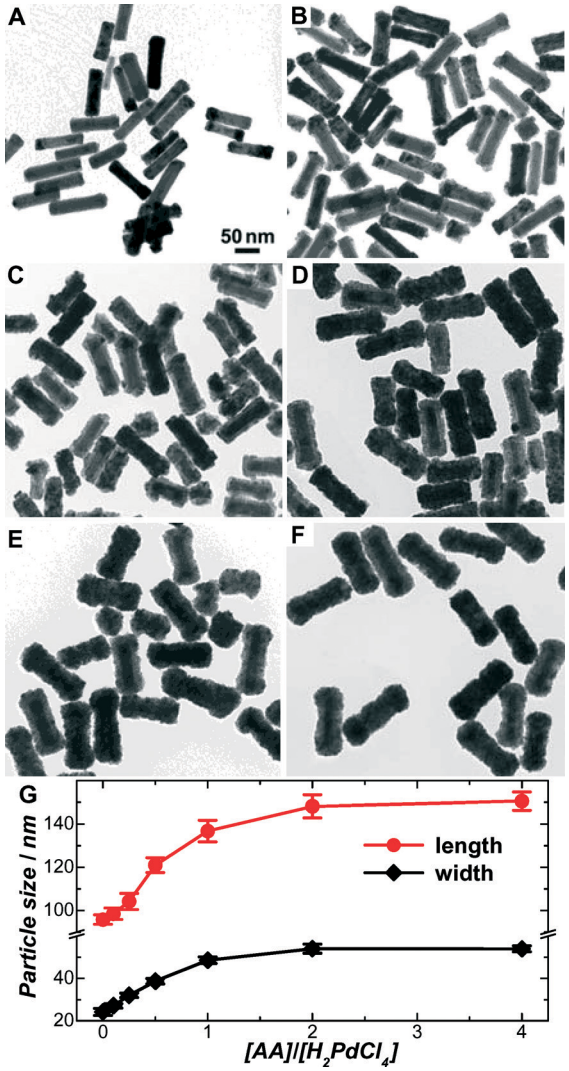

Fig. 3 TEM images of Au@Pd core–shell nanorods with polycrystalline Pd shells obtained in CTAC at various AA to H_2PdCl_4 ratios of (A) 0.1, (B) 0.25, (C) 0.5, (D) 1.0, (E) 2.0 and (F) 4.0. All the TEM images share the same scale bar in panel A. (G) Evolution of the width and length of the core–shell nanorods as the ratio of AA to H_2PdCl_4 varies.

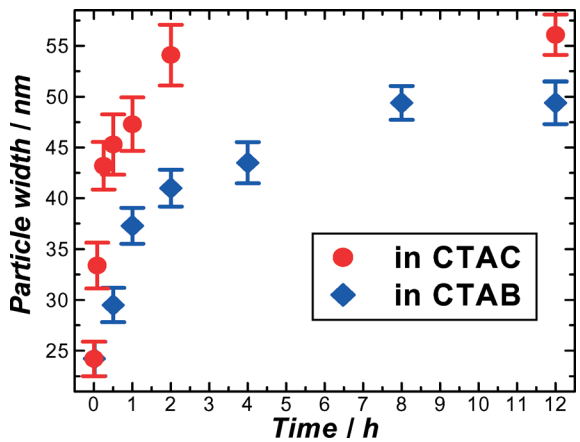

Fig. 2 Evolution of the particle width at various reaction times during the Pd overgrowth on Au nanorods in CTAC and CTAB at 30 °C. The molar ratio of AA to H_2PdCl_4 was 1.0.

3.3 Optical properties of Au@Pd core–shell nanostructures

The overgrowth of the Pd shells on Au nanorods introduced significant changes to the plasmon resonance frequencies and extinction spectral line-shapes of the particles. The optical properties of the Au@Pd core–shell nanostructures were strongly dependent on both the thickness and morphology of the Pd shells. As shown in Fig. 5A, the longitudinal plasmon resonance progressively red-shifted as the thickness of the polycrystalline Pd shell increased while the traverse plasmon mode was much less sensitive to the shell thickness. The red-shift of the plasmon resonances of the Au@Pd core–shell nanorods with respect to that of the bare Au nanorods is due to the dielectric nature of the discontinuous Pd shells, which have a positive real part of the dielectric function.[27] Significant broadening of the plasmon resonance peaks and increased

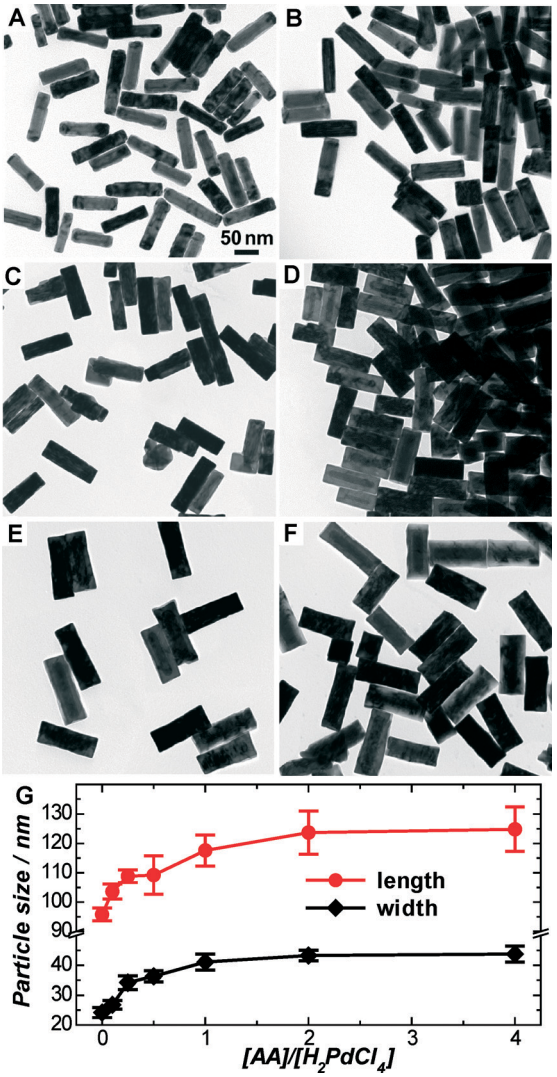

Fig. 4 TEM images of Au@Pd core–shell nanocuboids with single-crystalline Pd shells obtained in CTAB at various AA to H_2PdCl_4 ratios of (A) 0.1, (B) 0.25, (C) 0.5, (D) 1.0, (E) 2.0 and (F) 4.0. All the TEM images share the same scale bar in panel A. (G) Evolution of the width and length of the core–shell nanocuboids as the ratio of AA to H_2PdCl_4 varies.

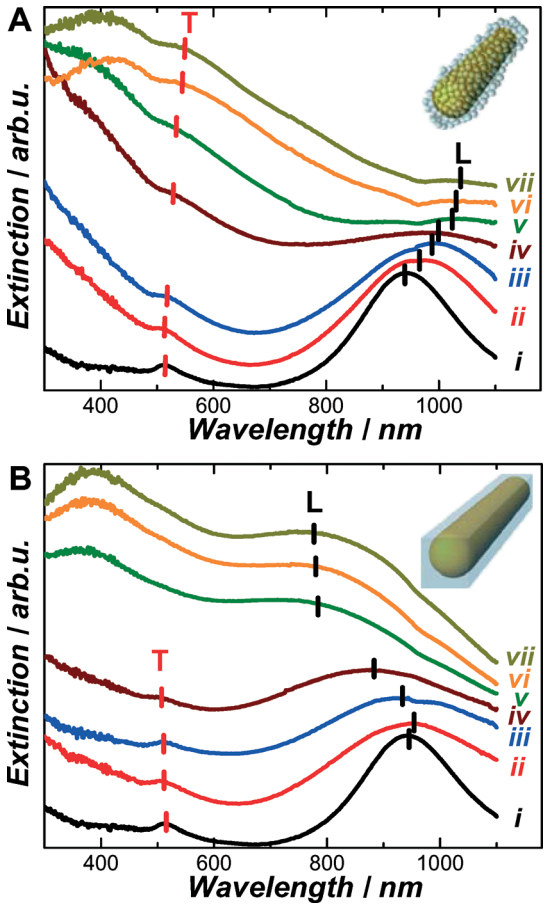

Fig. 5 Optical extinction spectra of (A) Au nanorods coated with polycrystalline Pd shells and (B) Au@Pd core–shell nanocuboids with single-crystalline Pd shells obtained at AA to H_2PdCl_4 ratios of (ii) 0.1, (iii) 0.25, (iv) 0.5, (v) 1.0, (vi) 2.0, and (vii) 4.0. Spectrum (i) in each panel is for the bare Au nanorods. The longitudinal and transverse plasmon modes are labelled as L and T, respectively.

optical extinction in the short-wavelength region below ~650 nm were also observed as the thickness of the polycrystalline Pd shells increased due to the plasmon damping and light absorption enhancement caused by the interband transitions of the Pd shells.[20]

In striking contrast to the Au nanorods coated with polycrystalline Pd shells, the plasmon resonances of the Au@Pd core–shell nanocuboids blue-shifted as the shell thickness increased (see Fig. 5B). Continuous Pd shells are metallic in nature with a negative real part of their dielectric functions. Therefore, coating the Au nanorods with a continuous Pd shell gave rise to the blue-shift of the plasmon resonances. As the thickness of the conformal Pd shell increased, plasmon damping became increasingly more significant as the longitudinal plasmon bands became broader and less distinguishable in the extinction spectra. It was recently observed that plasmonic percolation occurred on Au@Pd core–shell nanorods when discontinuous Pd islands started to merge into a continuous conformal shell. The transition of Pd from a dielectric shell to a metallic shell occurred when a threshold volume packing density of ~70% was reached.[27] Our extinction spectroscopic results can be well interpreted in the context of this plasmonic percolation picture.

3.4 Effects of reaction temperatures on the nanoparticle morphologies

We have also examined the effects of reaction temperature on the overgrowth of Pd on Au nanorods. As illustrated in Fig. 6A, Au@Pd core–shell nanorods with irregular shapes were obtained in the presence of CTAC when the reaction temperature was increased to 60 °C. TEM images in Fig. 6B–E show that these irregularly shaped core–shell nanorods have a continuous Pd shell surrounding each Au nanorod core. Moiré patterns were clearly observed in the core regions of the particles. Increasing AA to H_2PdCl_4 ratio led to the formation of thicker Pd shells. Higher reaction temperatures helped

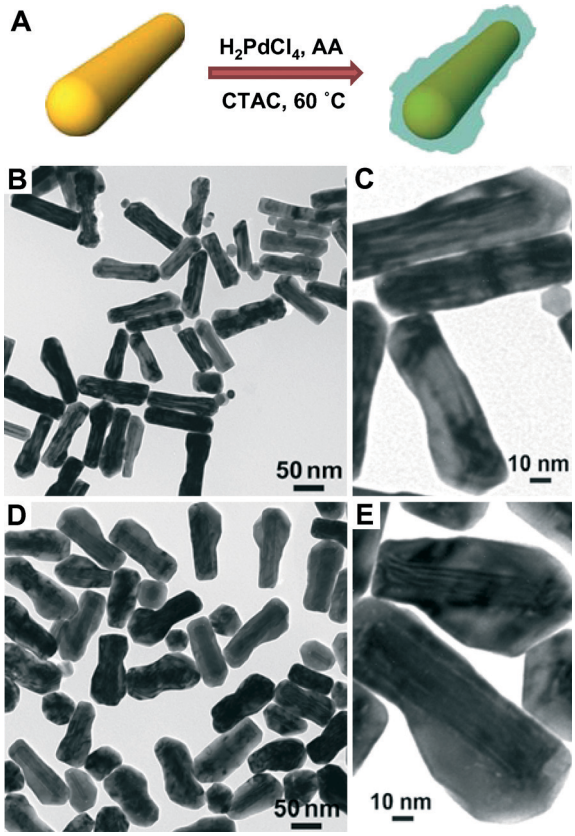

Fig. 6 (A) Schematic illustration of the formation of irregularly shaped Au@Pd core–shell nanorods at 60 °C in the presence of CTAC. TEM images of irregularly shaped core–shell nanorods produced at AA to H_2PdCl_4 ratios of (B, C) 0.25 and (D, E) 0.5.

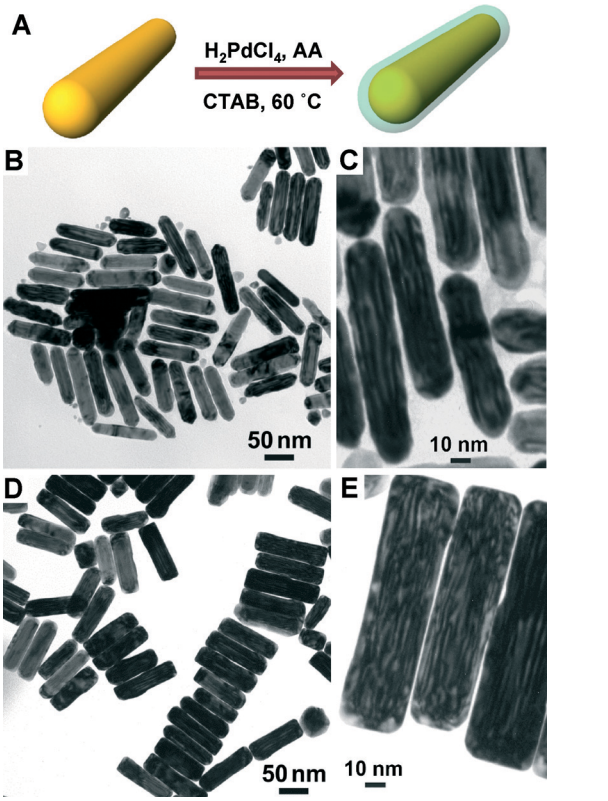

Fig. 7 (A) Schematic illustration of the formation of Au@Pd co-axial core–shell nanorods at 60 °C in the presence of CTAB. TEM images of Au@Pd co-axial core–shell nanorods fabricated at AA to H_2PdCl_4 ratios of (B, C) 0.25 and (D, E) 0.5.

overcome the energy barrier caused by the lattice mismatch between the core and the shell and thus favoured the formation of continuous Pd shells during the Pd overgrowth process. Unlike CTAB, CTAC may lack the capability to specifically stabilize a particular crystalline facet. Therefore, core–shell nanorods with irregularly shaped morphology were obtained.

When using CTAB as the surface capping agent, Au@Pd co-axial nanorods with a cylindrical morphology were obtained at 60 °C, as illustrated in Fig. 7A. It has been reported that the side surfaces of the single-crystalline Au nanorods are enclosed by both {100} and {110} facets.[31] At 30 °C, the Pd shell grew faster along the [110] direction than the [100] direction due to the strong stabilization of the {100} facets by CTAB,[17,18,31,34] giving rise to the formation of nanocuboids enclosed by {100} facets. However, when the reaction temperature increased to 60 °C, the Pd growth rates along [110] and [100] directions both increased and became comparable. Therefore, the cylindrical shape of the Au nanorod cores was preserved during the overgrowth process as shown by Fig. 7B–E. Interestingly, the Moiré patterns were observed throughout the whole cross-sections of the nanoparticles (Fig. 7C and E). This is possibly due to the lattice mismatch both between the Au core and the Pd shell and at the boundaries between the Pd domains that were expitaxially grown on the Au {100} and {110} facets.

3.5 Effects of Ag^+ on the Pd overgrowth on Au nanorods

Foreign ions, such as Ag^+, play crucial roles in the shape control of various Au nanostructures, such as cylindrical nanorods,[25] nanotetrahexahedra,[40] and concave nanocubes,[41] during the seed-mediate growth processes. The underpotential deposition (UPD) of Ag results in the formation of a monolayer Ag on the surface of the seed particles,[42] which serves as shape-directing interfacial layer that guides the subsequent nanocrystal growth process *via* the selective surface passivation pathway.[42–44] It was recently reported that Ag^+ ions guided the growth of Pd satellite nanocrystal growth at specific sites on the Au nanooctahedral cores to form a large library of Au@Pd bimetallic heteronanostructures with very diverse architectures.[45,46] This strategy took advantage of the galvanic replacement reaction of a sustainably regenerated Ag UPD layer on a central Au nanooctahedron to generate geometry-dependent heterogeneous distributions of electrons, which was further coupled with the manipulation of crystal growth kinetics to achieve shape and size control of satellite nanocrystals in a site-selective manner. Here we explored the effects of Ag^+ on the overgrowth of Pd on Au nanorods. In a typical synthesis, Ag^+ and H_2PdCl_4 were introduced simultaneously into the colloidal Au nanorods in the presence of CTAC or CTAB at 30 °C, followed by the addition of the AA as the reducing

agent to initiate the Ag-UPD guided deposition of Pd (Fig. 8A). Under these circumstances, discontinuous Pd shells composed of segregated nanoislands were deposited on Au nanorods as shown in Fig. 8.

During the Ag^+-mediated Pd overgrowth, a sub-monolayer of Ag was first deposited on the Au nanorods through a fast UPD process. Then this *in situ* generated Ag UPD layer was consumed by galvanic replacement reaction with the $PdCl_4^{2-}$ ions in the solution and this UPD layer could be continuously regenerated due to an abundant supply of reducing agent, AA, in the solution. Pd shells with rough surfaces composed of segregated islands formed gradually due to the presence of lattice vacancies created during the continuous galvanic replacement reaction.[47,48] Overall, the crystal overgrowth was propelled by the co-reduction and co-deposition of Ag and Pd concurrent with the galvanic replacement reaction.[45,46] The sustainable generation of the Ag UPD-layer on the surface of newly reduced Pd layer and the subsequent galvanic replacement reaction were essential for the formation of Pd shells composed of segregated nanoislands on the Au nanorods. As shown in Fig. S5 and S6 in ESI,† the EDS analysis verified the presence of Ag in the Pd shell structures for both samples synthesized in CTAC and CTAB.

The morphology of the Pd shells was found to be strongly dependent on the concentration of Ag^+ in the presence of CTAB as the surface capping agent. Continuous conformal Pd shells were overgrown on the Au nanorods in the absence of Ag^+ or at low Ag^+ concentrations (Fig. 9A). As the Ag^+ concentration progressively increased, small cavities started to form at the Au–Pd interfaces (Fig. 9B) most likely due to the galvanic replacement of the Ag UPD layer by Pd. At sufficiently high Ag^+ concentrations, segregated Pd islands started to form on the Au nanorods (Fig. 9C). The plasmon percolation behaviour was observed as the continuous Pd shells were transformed into discontinuous Pd nanoislands when the Ag^+ concentration increased (Fig. 9D).

Interestingly, dumbbell-like Au@Pd core–shell nanoparticles were obtained when H_2PdCl_4 and AA were added into the solution of pre-formed Au nanorods coated with a Ag UPD layer, as illustrated in Fig. 10A. In the first step, Ag^+ and AA were mixed with Au nanorods at 30 °C to deposit a Ag UPD layer on Au nanorods. Although it was difficult to visualize the ultrathin Ag UPD layers in TEM images (Fig. S7 in ESI†), the presence of Ag on Au nanorods was confirmed by EDS measurements as shown in Fig. S8 in ESI.† The blue-shift of longitudinal plasmon resonance peak in the extinction spectra for both samples synthesized in CTAC and CTAB (Fig. S9 in ESI†) provided additional evidence on the presence of Ag UPD layers on the Au nanorods.[34] After the Ag UPD was completed, Au–Ag bimetallic nanorods were centrifuged to remove the excessive Ag^+ ions, and then redispersed in the solution containing CTAC or CTAB, H_2PdCl_4, and AA to initiate the

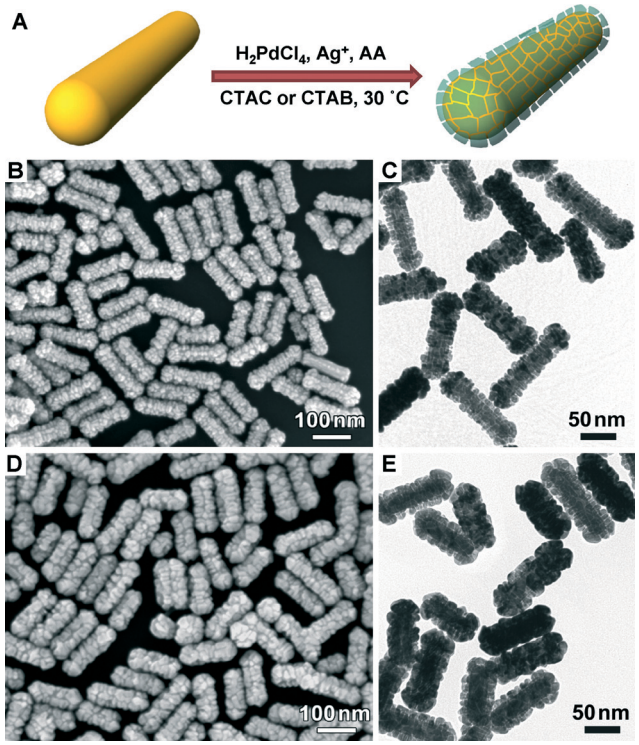

Fig. 8 (A) Schematic illustration of Ag^+-mediated overgrowth of segregated Pd islands on Au nanorods. (B) SEM and (C) TEM images of the heteronanostructures obtained through Ag^+-mediated Pd overgrowth on Au nanorods in CTAC. (D) SEM and (E) TEM images of the heteronanostructures obtained through Ag^+-mediated Pd overgrowth on Au nanorods in CTAB. The molar ratio of AA to H_2PdCl_4 was 0.5.

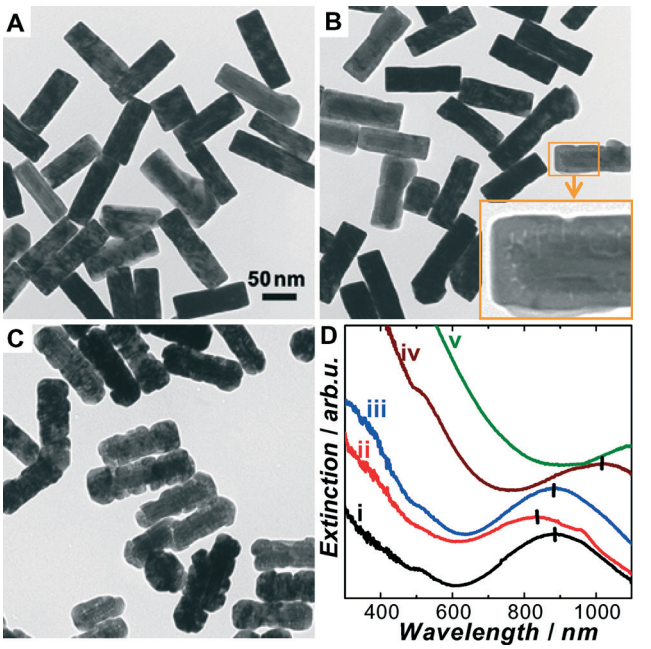

Fig. 9 TEM images of Au@Pd core–shell nanoparticles obtained through Ag^+-mediated Pd overgrowth in CTAB with (A) 20 μL, (B) 80 μL, and (C) 200 μL of 1 mM $AgNO_3$ added into the growth solution. (D) Extinction spectra of colloidal Au@Pd core–shell nanoparticles fabricated by adding (i) 0 μL, (ii) 20 μL, (iii) 80 μL, (iv) 200 μL, and (v) 400 μL of 1 mM $AgNO_3$ into the growth solution. The molar ratio of AA to H_2PdCl_4 was 0.5. All the TEM images share the same scale bar in panel A.

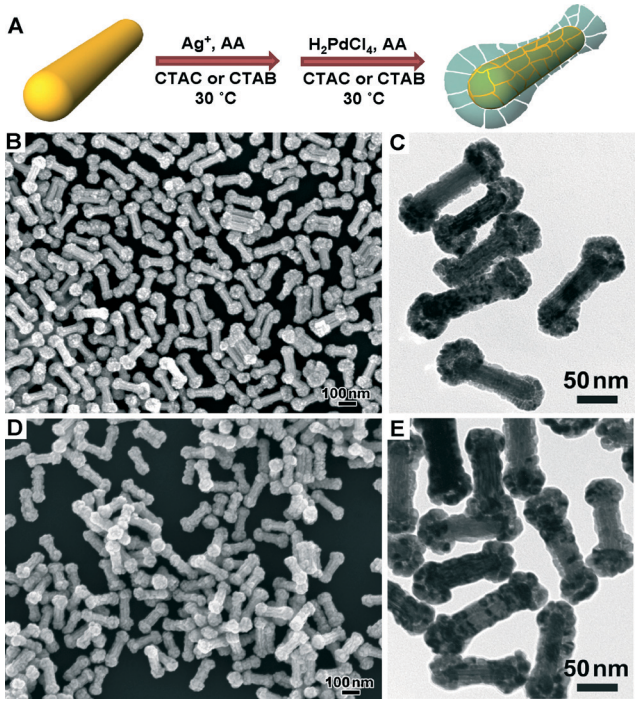

Fig. 10 (A) Schematic illustration of the formation of Au@Pd core–shell nanodumbbells. (B) SEM and (C) TEM images of Au@Pd core–shell nanodumbbells synthesized in CTAC. (D) SEM and (E) TEM images of Au@Pd core–shell nanodumbbells synthesized in CTAB. The molar ratio of AA to H_2PdCl_4 was 0.5.

overgrowth of Pd. We found that Pd was preferentially deposited at the two ends of the nanorod cores, giving rise to the formation of the dumbbell-shaped core–shell nanoparticles (Fig. 10B to E). Since the overgrowth of Pd was guided by the Ag UPD layers, the formation of the dumbbell-like nanostructures can be interpreted as a consequence of the preferential deposition of Ag UPD layers at the tips of the nanorods. It has been suggested that the packing density of CTAC or CTAB is higher on the side facets than on the tip facets of the Au nanorods.[38,49,50] Therefore, more Ag was deposited on the ends than on the side facets of the Au nanorods during the UPD of Ag, which favoured the subsequent overgrowth of Pd on the ends than on the lateral sides of the nanorods. When Ag^+ and H_2PdCl_4 were simultaneously introduced into the colloidal suspensions of pre-formed Au nanorods coated with Ag UPD layers (see Fig. S10 in ESI†), discrete Pd nanoislands were deposited evenly on both the end and side facets of the Au nanorod cores most likely due to the sustainable generation of the Ag UPD-layers on both the sides and ends of Au nanorods and the synergistic interplay effects of galvanic replacement and co-reduction-induced layer-by-layer deposition of Ag and Pd.

4. Conclusions

We have demonstrated that the controlled overgrowth of Pd on Au nanorods is governed by four important factors including the surface capping agents, molar ratio of AA to H_2PdCl_4, reaction temperature, and structure-directing foreign ions, such as Ag^+. Discrete polycrystalline Pd shells and conformal single-crystalline Pd shells were deposited on the surfaces of the Au nanorods at 30 °C using CTAC and CTAB as the surface capping agents, respectively. The thickness of polycrystalline and the conformal Pd shells were controlled by adjusting the molar ratio of AA to H_2PdCl_4. The capabilities to tightly control the thickness of the Pd shells allowed us to systematically study the effects of the shell dimensions and architectures on the optical properties of the core–shell nanoparticles. Raising the reaction temperature to 60 °C led to the formation of irregularly shaped Au@Pd core–shell nanorods in CTAC and cylindrical coaxial core–shell nanorods in CTAB, respectively. The effects of Ag^+ on the Pd overgrowth on Au nanorods were also investigated, which highlighted the importance of the sustainable Ag–UPD and galvanic replacements to the architectural control of Au@Pd core–shell heteronanostructures. Controlled overgrowth of Pd on Au nanorods provides a versatile approach to the optimization of the optical, electronic, and surface properties of the bimetallic core–shell heteronanostructures, enabling widespread applications in plasmonics, electronics, optoelectronics, and catalysis. The knowledge gained through this study provides useful information that may guide the rational design and controlled fabrication of multi-component hetero-nanostructures with increasing structural and compositional complexity.

Acknowledgements

This work was supported by a United States National Science Foundation Faculty Early Career Development (CAREER) Award (DMR-1253231). The authors thank the University of South Carolina Electron Microscopy Center for instrument use and technical assistance.

Notes and references

1 M. B. Cortie and A. M. McDonagh, *Chem. Rev.*, 2011, **111**, 3713–3735.
2 D. S. Wang and Y. D. Li, *Adv. Mater.*, 2011, **23**, 1044–1060.
3 S. E. Habas, H. Lee, V. Radmilovic, G. A. Somorjai and P. Yang, *Nat. Mater.*, 2007, **6**, 692–697.
4 D. V. Talapin, J. S. Lee, M. V. Kovalenko and E. V. Shevchenko, *Chem. Rev.*, 2010, **110**, 389–458.
5 Y. W. Lee, M. Kim, Z. H. Kim and S. W. Han, *J. Am. Chem. Soc.*, 2009, **131**, 17036–17037.
6 C. J. DeSantis and S. E. Skrabalak, *J. Am. Chem. Soc.*, 2013, **135**, 10–13.
7 J. Gu, Y. W. Zhang and F. Tao, *Chem. Soc. Rev.*, 2012, **41**, 8050–8065.
8 C. J. DeSantis, R. G. Weiner, A. Radmilovic, M. M. Bower and S. E. Skrabalak, *J. Phys. Chem. Lett.*, 2013, **4**, 3072–3082.
9 X. Q. Huang, Y. J. Li, Y. Chen, H. L. Zhou, X. F. Duan and Y. Huang, *Angew. Chem., Int. Ed.*, 2013, **52**, 6063–6067.
10 P. P. Fang, A. Jutand, Z. Q. Tian and C. Amatore, *Angew. Chem., Int. Ed.*, 2011, **50**, 12184–12188.

11 C. Zhu, J. Zeng, J. Tao, M. C. Johnson, I. Schmidt-Krey, L. Blubaugh, Y. M. Zhu, Z. Z. Gu and Y. N. Xia, *J. Am. Chem. Soc.*, 2012, **134**, 15822–15831.
12 Y. Yu, Q. B. Zhang, B. Liu and J. Y. Lee, *J. Am. Chem. Soc.*, 2010, **132**, 18258–18265.
13 C. W. Yang, K. Chanda, P. H. Lin, Y. N. Wang, C. W. Liao and M. H. Huang, *J. Am. Chem. Soc.*, 2011, **133**, 19993–20000.
14 F. Wang, C. H. Li, L. D. Sun, H. S. Wu, T. A. Ming, J. F. Wang, J. C. Yu and C. H. Yan, *J. Am. Chem. Soc.*, 2011, **133**, 1106–1111.
15 C. L. Lu, K. S. Prasad, H. L. Wu, J. A. A. Ho and M. H. Huang, *J. Am. Chem. Soc.*, 2010, **132**, 14546–14553.
16 D. Y. Kim, S. W. Kang, K. W. Choi, S. W. Choi, S. W. Han, S. H. Im and O. O. Park, *CrystEngComm*, 2013, **15**, 7113–7120.
17 D. Y. Kim, K. W. Choi, X. L. Zhong, Z. Y. Li, S. H. Im and O. O. Park, *CrystEngComm*, 2013, **15**, 3385–3391.
18 F. R. Fan, D. Y. Liu, Y. F. Wu, S. Duan, Z. X. Xie, Z. Y. Jiang and Z. Q. Tian, *J. Am. Chem. Soc.*, 2008, **130**, 6949–6950.
19 C. J. DeSantis, A. A. Peverly, D. G. Peters and S. E. Skrabalak, *Nano Lett.*, 2011, **11**, 2164–2168.
20 F. Wang, L. D. Sun, W. Feng, H. J. Chen, M. H. Yeung, J. F. Wang and C. H. Yan, *Small*, 2010, **6**, 2566–2575.
21 B. Lim, H. Kobayashi, T. Yu, J. G. Wang, M. J. Kim, Z. Y. Li, M. Rycenga and Y. N. Xia, *J. Am. Chem. Soc.*, 2010, **132**, 2506–2507.
22 M. Tsuji, K. Ikedo, M. Matsunaga and K. Uto, *CrystEngComm*, 2012, **14**, 3411–3423.
23 C. J. Murphy, T. K. San, A. M. Gole, C. J. Orendorff, J. X. Gao, L. Gou, S. E. Hunyadi and T. Li, *J. Phys. Chem. B*, 2005, **109**, 13857–13870.
24 P. K. Jain, X. H. Huang, I. H. El-Sayed and M. A. El-Sayed, *Acc. Chem. Res.*, 2008, **41**, 1578–1586.
25 B. Nikoobakht and M. A. El-Sayed, *Chem. Mater.*, 2003, **15**, 1957–1962.
26 K. Zhang, Y. J. Xiang, X. C. Wu, L. L. Feng, W. W. He, J. B. Liu, W. Y. Zhou and S. S. Xie, *Langmuir*, 2009, **25**, 1162–1168.
27 H. J. Chen, F. Wang, K. Li, K. C. Woo, J. F. Wang, Q. Li, L. D. Sun, X. X. Zhang, H. Q. Lin and C. H. Yan, *ACS Nano*, 2012, **6**, 7162–7171.
28 F. Wang, C. H. Li, H. J. Chen, R. B. Jiang, L. D. Sun, Q. Li, J. F. Wang, J. C. Yu and C. H. Yan, *J. Am. Chem. Soc.*, 2013, **135**, 5588–5601.
29 J. F. Huang, Y. H. Zhu, M. Lin, Q. X. Wang, L. Zhao, Y. Yang, K. X. Yao and Y. Han, *J. Am. Chem. Soc.*, 2013, **135**, 8552–8561.
30 J. H. Song, F. Kim, D. Kim and P. D. Yang, *Chem. - Eur. J.*, 2005, **11**, 910–916.
31 Y. J. Xiang, X. C. Wu, D. F. Liu, X. Y. Jiang, W. G. Chu, Z. Y. Li, Y. Ma, W. Y. Zhou and S. S. Xie, *Nano Lett.*, 2006, **6**, 2290–2294.
32 M. Tsuji, K. Ikedo, K. Uto, M. Matsunaga, Y. Yoshida, K. Takemura and Y. Niidome, *CrystEngComm*, 2013, **15**, 6553–6563.
33 A. N. Wang, Q. Peng and Y. D. Li, *Chem. Mater.*, 2011, **23**, 3217–3222.
34 Q. Li, R. B. Jiang, T. Ming, C. H. Fang and J. F. Wang, *Nanoscale*, 2012, **4**, 7070–7077.
35 X. C. Ye, C. Zheng, J. Chen, Y. Z. Gao and C. B. Murray, *Nano Lett.*, 2013, **13**, 765–771.
36 D. B. Williams and C. B. Carter, *Transmission Electron Microscopy, a Text for Materials Science*, Plenum Press, New York, 1996.
37 M. Grzelczak, B. Rodriguez-Gonzalez, J. Perez-Juste and L. M. Liz-Marzan, *Adv. Mater.*, 2007, **19**, 2262–2266.
38 B. Nikoobakht and M. A. El-Sayed, *Langmuir*, 2001, **17**, 6368–6374.
39 X. Guo, Q. Zhang, Y. H. Sun, Q. Zhao and J. Yang, *ACS Nano*, 2012, **6**, 1165–1175.
40 T. Ming, W. Feng, Q. Tang, F. Wang, L. D. Sun, J. F. Wang and C. H. Yan, *J. Am. Chem. Soc.*, 2009, **131**, 16350–16351.
41 J. Zhang, M. R. Langille, M. L. Personick, K. Zhang, S. Y. Li and C. A. Mirkin, *J. Am. Chem. Soc.*, 2010, **132**, 14012–14014.
42 M. Z. Liu and P. Guyot-Sionnest, *J. Phys. Chem. B*, 2005, **109**, 22192–22200.
43 M. R. Langille, M. L. Personick, J. Zhang and C. A. Mirkin, *J. Am. Chem. Soc.*, 2012, **134**, 14542–14554.
44 M. L. Personick, M. R. Langille, J. Zhang and C. A. Mirkin, *Nano Lett.*, 2011, **11**, 3394–3398.
45 Y. Yu, Q. B. Zhang, J. P. Xie and J. Y. Lee, *Nat. Commun.*, 2013, **4**, 1454.
46 Y. Yu, Q. B. Zhang, Q. F. Yao, J. P. Xie and J. Y. Lee, *Chem. Mater.*, 2013, **25**, 4746–4756.
47 Y. G. Sun and Y. N. Xia, *J. Am. Chem. Soc.*, 2004, **126**, 3892–3901.
48 X. H. Xia, Y. Wang, A. Ruditskiy and Y. N. Xia, *Adv. Mater.*, 2013, **25**, 6313–6333.
49 L. F. Gou and C. J. Murphy, *Chem. Mater.*, 2005, **17**, 3668–3672.
50 Z. L. Wang, M. B. Mohamed, S. Link and M. A. El-Sayed, *Surf. Sci.*, 1999, **440**, L809–L814.